

Anomalous Enhancement of the Electrocatalytic Hydrogen Evolution Reaction in AuPt Nanoclusters

Jiahui Kang,¹ Jan Kloppenburg,² Jiali Sheng,¹ Zhenyu Xu,¹ Kristoffer Meinander,³ Hua Jiang,¹ Zhong-Peng Lv,¹ Esko I. Kauppinen,¹ Qiang Zhang,¹ Xi Chen,^{1,4,5} Olli Ikkala,¹ Miguel A. Caro,^{2,*} and Bo Peng^{1,6,†}

¹Department of Applied Physics, Aalto University, 02150, Espoo, Finland

²Department of Chemistry and Materials Science, Aalto University, 02150, Espoo, Finland

³Department of Bioproducts and Biosystems, Aalto University, 02150, Espoo, Finland

⁴School of Physical Science and Technology, Lanzhou University, Lanzhou, Gansu 730000, China

⁵Lanzhou Center for Theoretical Physics and Key Laboratory for Quantum Theory and Applications of the Ministry of Education, Lanzhou University, Lanzhou, Gansu 730000, China

⁶Department of Materials Science, Advanced Coating Research Center of Ministry of Education of China, Fudan University, Shanghai 200433, China

(Dated: June 14, 2024)

Abstract

Energy- and resource-efficient electrocatalytic water splitting is of paramount importance to enable sustainable hydrogen production. The best bulk catalyst for the hydrogen evolution reaction (HER), i.e., platinum, is one of the scarcest elements on Earth. The use of raw material for HER can be dramatically reduced by utilizing nanoclusters. In addition, nanoalloying can further improve the performance of these nanoclusters. In this paper, we present results for HER on nanometer-sized ligand-free AuPt nanoclusters grafted on carbon nanotubes. These results demonstrate excellent monodispersity and a significant reduction of the overpotential for the electrocatalytic HER. We utilize atomistic machine learning techniques to elucidate the atomic-scale origin of the synergistic effect between Pt and Au. We show that the presence of surface Au atoms, known to be poor HER catalysts, in a Pt(core)/AuPt(shell) nanocluster structure, drives an anomalous enhancement of the inherently high catalytic activity of Pt atoms.

I. INTRODUCTION

With the expansion of industry and the growth of the world population, the demand for energy from non-renewable fossil fuels has increased significantly, inevitably generating large amounts of carbon emissions and thus causing climate change and energy scarcity [1–4]. Hydrogen is considered as one of the most essential clean and renewable energy sources for alternative high-efficiency energy conversion and storage technologies, especially when coupled to green electricity from such renewable resources as wind, tidal, and solar [5]. Water is the most readily accessible source of hydrogen. Thus, energy-efficient electrocatalytic water splitting is the most attractive way to produce hydrogen. The hydrogen evolution reaction (HER) is a key half-reaction of water splitting on the cathode, which involves multi-step reactions, hindering the efficiency of water splitting. Therefore, the availability of high-efficiency catalysts for HER is critical for accelerating the sluggish reaction and decreasing the dynamic overpotential [5–8]. Currently, noble metal-based materials are the most widely used to decrease the overpotential, such as Pt-based catalysts for HER [9–11]. Due to their cost and scarcity, reducing the amount of raw material is of paramount importance when utilizing Pt and other noble metals. For this reason, replacing bulk catalysts with their nanostructured forms is a widely explored strategy. Pt-based nanoparticles have been studied for many years as a means to decrease the usage of raw Pt and improve the efficiency and stability of Pt-based catalysts for

HER [9, 10].

Thanks to the small size and large specific area of nanoclusters (NCs), which involve monodispersity, NCs are expected to have more active catalytic sites than bulkier nanoparticles, making them a promising nanomaterial for water splitting catalysis. Moreover, compared with nanoparticles, the electronic structure and properties of NCs are more strongly dependent on the applied potential [12–14]. The size, morphology and composition of NCs are the three key factors affecting their properties [15–20]. With regard to composition, alloyed NCs are designed to improve the physicochemical activity because of the possible synergistic effects in multi-metallic NCs, where the properties of the alloy differ from the properties of the mono-metallic constituents [15, 16, 21–24]. For instance, Pt/Pd-doped MAu(SR)₁₈ gold NCs, where R is the ligand, were extensively studied in recent years because of the interesting alloying effect that regulates the geometry, structure and physicochemical properties, including thermal stability, reactivity, catalytic performance, and magnetism [25–27].

In this paper, we show that alloying Pt NCs, which are intrinsically catalytically active towards HER [9, 10], with Au, which is catalytically inactive for the same reaction, allows the formation of bimetallic NCs with superior and tunable catalytic activity.

Another important consideration is the tradeoff between NC activity and stability, because in industrial-scale applications the active materials need to remain catalytically active for extended periods of time to be economically viable. Ligand-protected NCs are stable but insufficiently efficient for catalysis. Removing the catalytically inert ligand of NCs by annealing is an effective way to improve their performance [28]. However, the NCs can aggregate after ligand removal and suf-

* mcaroba@gmail.com

† pengbo006@gmail.com

fer from instability during the electrocatalytic process. Grafting the NCs to a stable support, e.g., conductive carbon, is a widely accepted way to prevent the aggregation of ligand-free NCs by immobilizing them on the support [29]. Carbon nanotubes (CNTs) are an attractive support for electrocatalysis because of their unique structure and intrinsic properties such as high surface area, high chemical stability, high electrical conductivity, and insolubility in most solvents [30, 31]. In this work, we precisely regulate the catalytic activity by optimizing the Au:Pt ratio of Pt (core)-AuPt (shell) NCs to increase the number of active sites and enhance the intrinsic activity towards HER. The NCs are grafted to CNT substrates to facilitate the electric conductivity and prevent agglomeration. The ligand-free $\text{Au}_{0.4}\text{Pt}_{0.6}$ NC-CNT-A (where A stands for annealed) complex shows the highest HER activity among all studied NC-CNT complexes, with an overpotential (η) of 27 mV at 10 mA cm^{-2} , a high mass activity of 7.49 A mg^{-1} at $\eta = 100 \text{ mV}$, and a high turnover frequency (TOF) of 7.63 s^{-1} , outperforming the majority of reported Pt-based catalysts to date.

To provide a mechanistic understanding of the origin of this anomalous enhancement, we resort to combining the experimental results with atomistic simulation [1]. We carry out simulated-annealing molecular dynamics (MD) simulations with a custom-made machine learning potential (MLP) for AuPt:H to elucidate the nature of the ligand-free AuPt NC structure. This analysis reveals a strong surface segregation of Au atoms and consequent core (Pt)-shell (AuPt) structure of the annealed AuPt NCs. We also perform heuristic Markov-chain grand-canonical Monte Carlo (GCMC) simulations at variable (electro) chemical potential. These suggest that, despite their low intrinsic activity, the presence of Au atoms drives an enhancement of H adsorption on neighboring Pt atoms. In addition to providing a mechanistic understanding of the H-adsorption process and its interplay with the AuPt alloy nanostructure, these simulations predict, in full agreement with the experimental observations, that H adsorption is more favorable on AuPt at a low Au fraction than in pure Pt, resulting in excellent catalytic performance for HER. This enhanced activity stems from the ability of the exposed adsorption Pt sites on the NC surface to bind hydrogen at higher electrode potential in the presence of neighboring Au atoms. This cooperative enhancement is “anomalous” in the sense that it follows the opposite trend that would be expected from interpolating between the behavior of pure ligand-free Pt NCs (excellent HER catalysts) and pure ligand-free Au NCs (poor HER catalysts).

II. EXPERIMENTAL SECTION

A. Preparation of AuPt nanoclusters and AuPt-CNT-A

Chemicals and materials: L-glutathione (GSH) in the reduced form ($\geq 98.0 \%$, Sigma-Aldrich), sulfuric acid (puriss., Sigma, 95-97 %), chloroplatinic acid hexahydrate ($\text{H}_2\text{PtCl}_6 \cdot 6\text{H}_2\text{O}$, ACS, $\geq 37.50 \%$ Pt basis, Sigma), gold(III) chloride trihydrate ($\text{HAuCl}_4 \cdot 3\text{H}_2\text{O}$, $\geq 99.9 \%$ trace metals

basis, Sigma), dialysis membrane (3.5 kD).

Synthesis of the (ligand-protected) $\text{Au}_{0.4}\text{Pt}_{0.6}$ NCs: The NCs were prepared following the protocol of Ref. [32] for pure Au NCs but adjusting the ratio of Au and Pt precursors according to the desired final NC stoichiometry (0.4/0.6 feed ratio for $\text{Au}_{0.4}\text{Pt}_{0.6}$). The NCs with other compositions had their feed ratios modified accordingly.

Synthesis of the (ligand-protected) $\text{Au}_{0.4}\text{Pt}_{0.6}$ -CNT film: The H_2SO_4 -processed CNT films were put into 2 mL $\text{Au}_{0.4}\text{Pt}_{0.6}$ NCs dispersion for 20 h.

Synthesis of (ligand-free) $\text{Au}_{0.4}\text{Pt}_{0.6}$ -CNT-A film: An $\text{Au}_{0.4}\text{Pt}_{0.6}$ -CNT film was put into a tube furnace at $300 \text{ }^\circ\text{C}$ for 30 min annealing under N_2 protection. After annealing, the $\text{Au}_{0.4}\text{Pt}_{0.6}$ -CNT-A film was prepared.

B. Structural characterization of AuPt nanoclusters and AuPt-CNT-A

The transmission electron microscopy (TEM) characterizations and energy dispersive X-ray spectroscopy (EDS) mapping were performed on a JEOL JEM-2200FS operated at 200 kV. All particle size distributions are calculated based on a count of ~ 100 particles. The X-ray diffraction (XRD) patterns were recorded using the Rigaku Smart Lab X-ray diffractometer with $\text{Cu-K}\alpha$ radiation. The small angle X-ray scattering (SAXS) and wide-angle X-ray scattering (WAXS) measurements were conducted by Xenocs Xeuss 3.0. The surface component measurements were performed with a Kratos AXIS Ultra DLD X-ray photoelectron spectrometer (XPS) using a monochromated $\text{Al-K}\alpha$ X-ray source (1486.7 eV) run at 100 W. All CNT spectra were charge-corrected relative to the position of the graphitic carbon at a binding energy of 284.2 eV. XPS of the ligand-protected AuPt NCs without CNT is measured after that the solutions were freeze-dried to powders. All powder spectra were also charge-corrected relative to the position of C-C bonding at a binding energy of 284.8 eV. The inductively coupled plasma-optical emission spectroscopy (ICP-OES) test was performed using an Agilent 730 series ICP optical emission spectrometer to determine the actual Au and Pt element contents. Fourier-transform infrared spectroscopy (FTIR) was performed with a PerkinElmer FTIR with attenuated total reflectance (ATR). The X-ray absorption near-edge structure (XANES) was performed in transmission mode at the MAX IV Balder beamline, Sweden.

C. Electrochemical measurements

HER measurements were performed on a Metrohm Autolab electrochemical workstation at room temperature. CNT films with dimensions of $1 \times 0.2 \text{ cm}^2$ were used as the working electrode. Ag/AgCl (3 M KCl) and graphite rods were used as the reference and the counter electrodes (RE and CE), respectively. The Ag/AgCl electrode was calibrated with respect to a reversible hydrogen electrode (RHE). The sample surface area for electrochemical test is 0.2 cm^2 . The HER measurement

was carried out in an N_2 -saturated 0.5 M H_2SO_4 aqueous solution. Linear sweep voltammetry (LSV) was conducted at a scan rate of 5 mV s^{-1} . The stability test was performed at a current density of 10 mA cm^{-2} for 24 h within the N_2 -saturated 0.5 M H_2SO_4 aqueous solution. The electrochemical surface area (ECSA) measurements were conducted at a potential between 0.2 and 0.4 V versus RHE. Electrochemical impedance spectroscopy (EIS) measurements were done from 100 kHz to 0.1 Hz. The LSV plots and chronoamperometric measurement are with IR compensation to eliminate the resistance overpotential. The IR compensation can be expressed by the following equation: $E_{\text{corrected}} = E_{\text{uncorrected}} - I \times R$ [33].

III. RESULTS AND DISCUSSION

A. Synthesis and morphologies of AuPt-CNT-A

The ligand-free AuPt-CNT-A was synthesized by the following steps: 1) synthesis of the ligand-protected AuPt nanoclusters; 2) ligand-protected AuPt NCs grafted onto the CNTs and 3) annealing, as schematically shown in Fig. 1a. To elucidate the morphology of the CNTs before and after processing, transmission electron microscopy (TEM) characterization was performed. The characteristics of the pristine CNTs (before processing) are summarized in Fig. S1. The pristine CNTs are grown by nucleation on Fe nanoparticles, formed from the decomposition of the ferrocene precursor. These Fe nanoparticles are encapsulated by uniform graphitic carbon layers (Fig. S1c), with interlayer spacing $d(002) = 0.32\text{--}0.36 \text{ nm}$ [34]. We further identify spacings of 0.206 nm of the particles could originate from the (110) plane of bcc Fe [35] or the (102) plane of Fe_3C [36], respectively. After washing with H_2SO_4 , the sulfated CNTs (Fig. S2c) retain their structure. The XRD patterns (Fig. S4) of the $Au_{0.4}Pt_{0.6}$ -CNT and $Au_{0.4}Pt_{0.6}$ -CNT-A samples show a series of broad Bragg peaks, suggesting low crystallinity of the of the grafted NCs and annealed NCs on CNT.

On the other hand, the TEM analysis shows a certain degree of crystallization of the ligand-free $Au_{0.4}Pt_{0.6}$ NCs on CNT film with annealing, as shown in Fig. 1b-d. The selected area electron diffraction (SAED) (Fig. 1c) demonstrates diffraction bright rings at d-spacings 2.04 Å and 1.02 Å, respectively, corresponding to the (200) and (400) plane of AuPt [37, 38], with other rings originated from the (110), (100), and (002) graphitic carbon, which is similar to the processed CNTs (Figure S3). The broad peaks in the XRD pattern are likely a consequence of the small size of the NCs [39]. The scanning transmission electron microscopy coupled energy-dispersive X-ray spectroscopy (STEM-EDS) element mapping in Fig. 1e shows the distribution of Au and Pt on the NCs across the selected area. For comparison, as shown in Fig. S5, the (ligand-protected) $Au_{0.4}Pt_{0.6}$ NCs as precursors are monodisperse with an average diameter of 1.5 nm (polydispersity index (PdI) = 0.025), suggesting the ligand stabilizes the structure of the NCs [32]. The (ligand-protected) $Au_{0.4}Pt_{0.6}$ NCs are amorphous, which can be confirmed by their SAED patterns (Fig. S5b). The EDS elemental mapping in Fig. S5d-h fur-

ther confirms the homogeneous distribution of both Au and Pt elements in $Au_{0.4}Pt_{0.6}$ NCs. After grafting, the (ligand-protected) $Au_{0.4}Pt_{0.6}$ NCs are monodispersed on the CNTs ($\sim 1.54 \text{ nm}$, PdI = 0.047), as shown in Fig. S6. Furthermore, after annealing, as shown in Fig. S7, the (ligand-free) $Au_{0.4}Pt_{0.6}$ NCs ($\sim 1.68 \text{ nm}$, PdI = 0.036) are still monodispersely distributed over the CNT matrix with a narrow size distribution (Fig. 1f), and the sizes are almost unchanged in comparison to the (ligand-protected) $Au_{0.4}Pt_{0.6}$ NCs on CNT prior to annealing.

B. WAXS and SAXS characterizations

In order to further obtain the structural features (size and shape) of the NCs on CNTs, small angle X-ray scattering (SAXS) and wide angle X-ray scattering (WAXS) experiments were performed on the (ligand-free) $Au_{0.4}Pt_{0.6}$ -CNT-A film, (ligand-protected) $Au_{0.4}Pt_{0.6}$ -CNT film, CNT film and (ligand-protected) $Au_{0.4}Pt_{0.6}$ NCs (Figs. 1g, S8 and S9, and Table S1). A log-normal distribution of diameters was used to fit the WAXS data. The average diameters $\langle d \rangle$ of the NCs obtained thereof are shown in Table S1. The value of 2.80 Å in $Au_{0.4}Pt_{0.6}$ -CNT and $Au_{0.4}Pt_{0.6}$ NCs shows the typical distance between Au and Pt atoms in an NC. The distances of 2.33 Å and 2.04 Å in $Au_{0.4}Pt_{0.6}$ -CNT-A can be assigned to the lattice spacings of the (111) and (200) planes of AuPt, respectively, which indicate a certain degree of AuPt crystallization after annealing, which is consistent with TEM [37, 38]. It is worth noting that the distance of 3.58 Å in $Au_{0.4}Pt_{0.6}$ -CNT-A corresponds to the interlayer spacing in graphitic carbon. This peak becomes apparent only after annealing, possibly because of the shift (and splitting) of the partly overlapping AuPt peak. From the Kratky plot (Figure S9a), $Au_{0.4}Pt_{0.6}$ -CNT shows a peak around 1.83 nm, suggesting that this is the average distance between AuPt NCs distributed on the CNTs. After removing the ligand, $Au_{0.4}Pt_{0.6}$ -CNT-A shows 3.63 nm for the distance between the NCs, which suggests AuPt NCs migration on the CNTs during annealing. The SAXS data in Fig. S9b indicates the average separation between CNTs in the CNT bundles is expanded from 33 nm to >50 nm after deposition of the NCs.

C. Atomistic structure and XPS characterization

To determine the atomistic structure of $Au_{0.4}Pt_{0.6}$ -CNT-A, the chemical composition was further examined by X-ray photoelectron spectroscopy (XPS) analysis. The XPS of CNT films as the substrate is shown in Fig. S10. The survey spectra of (ligand-protected) $Au_{0.4}Pt_{0.6}$ NCs, (ligand-protected) $Au_{0.4}Pt_{0.6}$ -CNT, and (ligand-free) $Au_{0.4}Pt_{0.6}$ -CNT-A shown in Fig. S11 confirm the presence of Au, Pt, C, N, S, and O elements and similar chemical composition of the $Au_{0.4}Pt_{0.6}$ NCs and the grafted nanoclusters ($Au_{0.4}Pt_{0.6}$ -CNT). The normalization of XPS peaks by their relative sensitivity factors yielded the average composition of $Au_{0.4}Pt_{0.6}$ NCs, $Au_{0.4}Pt_{0.6}$ -CNT, and $Au_{0.4}Pt_{0.6}$ -CNT-A and is shown in Table S2. The in-

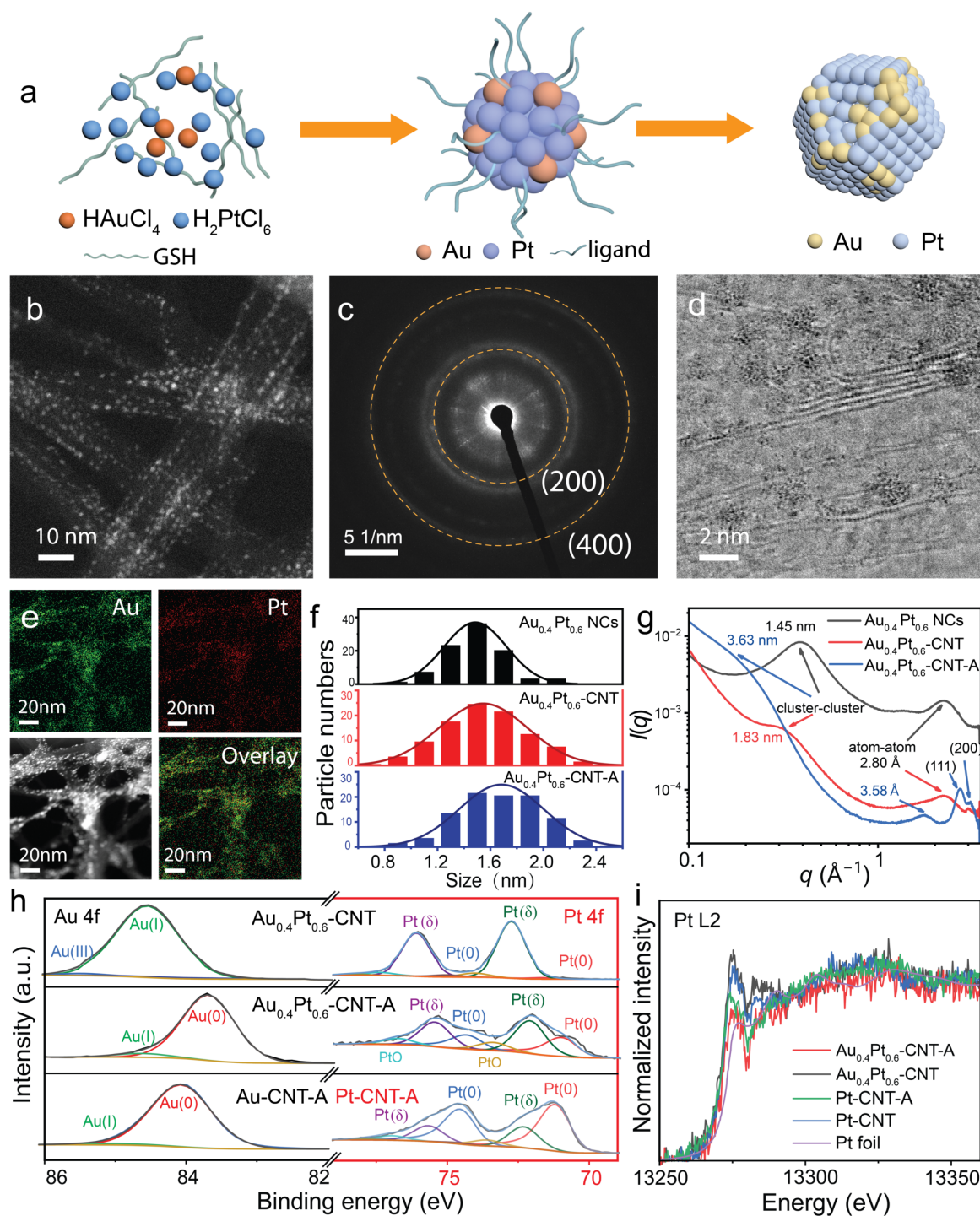


FIG. 1. a) Schematics of the preparation of AuPt NCs on CNT with annealing. b) High-angle annular dark-field scanning transmission electron microscopy (HAADF-STEM) image of $\text{Au}_{0.4}\text{Pt}_{0.6}\text{-CNT-A}$, and the corresponding c) Selected area electron diffraction (SAED) patterns of $\text{Au}_{0.4}\text{Pt}_{0.6}$ nanoclusters on CNT with annealing. d) High-angle annular bright-field scanning transmission electron microscopy (HAABF-STEM) image of $\text{Au}_{0.4}\text{Pt}_{0.6}\text{-CNT-A}$. e) STEM-EDS (energy dispersive X-ray spectroscopy) elemental mapping of $\text{Au}_{0.4}\text{Pt}_{0.6}\text{-CNT-A}$. f) Corresponding particle size statistics and g) wide-angle X-ray scattering (WAXS) results of $\text{Au}_{0.4}\text{Pt}_{0.6}$ NCs, $\text{Au}_{0.4}\text{Pt}_{0.6}\text{-CNT}$, and $\text{Au}_{0.4}\text{Pt}_{0.6}\text{-CNT-A}$. h) Au 4f and Pt 4f XPS of the grafted $\text{Au}_{0.4}\text{Pt}_{0.6}\text{-CNT}$, and $\text{Au}_{0.4}\text{Pt}_{0.6}\text{-CNT-A}$ film, Au 4f XPS spectra of pure Au-CNT-A film, and Pt 4f XPS spectra of with pure Pt-CNT-A film. i) Normalized X-ray absorption near-edge structure (XANES) spectra at Pt L₂-edge of $\text{Au}_{0.4}\text{Pt}_{0.6}\text{-CNT-A}$ and $\text{Au}_{0.4}\text{Pt}_{0.6}\text{-CNT}$, Pt-CNT-A, Pt-CNT and Pt foil.

creased C/O ratio after annealing suggests the decrease of OH groups in Au_{0.4}Pt_{0.6}-CNT-A.

D. XPS characterization of the pristine ligand-protected Au_{0.4}Pt_{0.6} NCs

The Au 4f_{7/2} pattern of the Au_{0.4}Pt_{0.6} NCs (Fig. S12a and Table S3) can be deconvoluted to two peaks at 85.0 eV and 84.1 eV, which can be assigned to Au(III) and Au(I), respectively [32, 40]. The main peak of Pt 4f_{7/2} of the pristine Au_{0.4}Pt_{0.6} NCs (Fig. S12b) is at 72.2 eV, which belongs to Pt($\delta+$) ($0 < \delta < 2$) [41]. Also a small amount of Pt(0) was found in pristine Au_{0.4}Pt_{0.6} NCs [42]. Pristine Au_{0.4}Pt_{0.6} NCs with a high content of S for thiol (Fig. S11e, Tables S4 and S5) hints towards the formation of thiolate complexes [32]. The quantitative analysis indicates that, for pristine Au_{0.4}Pt_{0.6} NCs, ~ 20 % of the sulphur species with the dominant S 2p_{3/2} peak at 166.4 eV are oxidized S 2p components. The S 2p core level is characterized by two S 2p_{3/2} and S 2p_{1/2} spin-orbit split doublets. The dominant S 2p_{3/2} peak at 162.7 eV and accompanying S 2p_{1/2} peak at 163.8 eV can be assigned to thiolate groups, confirming the formation of AuPt-S thiolate bonds in pristine Au_{0.4}Pt_{0.6} NCs. According to previous research, ligand-protected Au NCs present a core-shell nanostructure with a Au(I)-thiolate complex as the shell and Au(0) as the core [32]. Based on these results and our XPS analysis, we speculate that the (ligand-protected) pristine Au_{0.4}Pt_{0.6} NCs have a similar core-shell nanostructure, i.e., Au(I)/Pt($\delta+$)-thiolate complex as the shell and Pt(0) as the core.

E. XPS characterization of grafted ligand-protected Au_{0.4}Pt_{0.6}-CNT

To further determine the location of Pt atoms of the NCs after being grafted onto the CNTs, the Au 4f_{7/2} and Pt 4f_{7/2} XPS spectra of the grafted Au_{0.4}Pt_{0.6}-CNT sample were measured. Again, the Pt 4f_{7/2} spectrum of grafted Au_{0.4}Pt_{0.6}-CNT can be deconvoluted into two peaks at 72.7 eV and 71.5 eV, where the latter can be assigned to Pt(0) [42] (Fig. 1h). Additionally, the peak position at 72.7 eV is at much lower energy than the reference Pt(II) peak, from which the 2+ valence state of Pt is expected to appear with a positive shift of +2.4 eV with respect to the Pt(0) peak. Therefore, it is reasonable to assign the peak at 72.7 eV to a state with intermediate valency Pt($\delta+$) ($0 < \delta < 2$) [41]. Besides, the grafted Au_{0.4}Pt_{0.6}-CNT shows a high content of S, attributed to the thiol groups from the surface complex, which also confirms that the Au_{0.4}Pt_{0.6} NCs on CNT are thiol-coated [41]. Moreover, the Au 4f peak at 84.5 eV exhibited a positive shift of ~ 0.4 eV, relative to 84.1 eV in pristine Au_{0.4}Pt_{0.6} NCs (Fig. S12 and Table S3). Similarly, positive shifts also appeared in Pt 4f, S 2p, N 1s, and O 1s of the grafted Au_{0.4}Pt_{0.6}-CNT compared with pristine Au_{0.4}Pt_{0.6} NCs (Fig. S11-12). These global shifts likely arise from sample charging during the XPS measurement and are not indicative of chemical changes in the NCs. To further elucidate the structure of the NCs on grafted Au_{0.4}Pt_{0.6}-CNT,

the XPS Au 4f_{7/2} and Pt 4f_{7/2} spectra of grafted pure Au-CNT and Pt-CNT, respectively, were both measured. As shown in Fig. S13, the Au 4f_{7/2} spectrum of the grafted pure Au-CNT can be deconvoluted into two peaks at 84.5 eV (Au(I)) and 84.0 eV (Au(0)), indicating that the NCs in the grafted pure Au-CNT samples also have an Au(I) core-Au(0) shell structure similar to that of the pristine Au NCs [32]. Moreover, Au(I) and Pt($\delta+$) peaks in Au_{0.4}Pt_{0.6}-CNT again reveal the formation of Au(I)/Pt($\delta+$)-thiolate complexes as the shell of the nanoclusters in Au_{0.4}Pt_{0.6}-CNT. Notably, the Au(0) (Fig. S13a) signal can hardly be observed in Au_{0.4}Pt_{0.6}-CNT, whilst an obvious Pt(0) (Fig. S13b) pattern is present in Au_{0.4}Pt_{0.6}-CNT, demonstrating that Pt(0) replaces the Au(0) core after adding Pt to Au-CNT [43]. Therefore, these results indicate a core-shell NC structure in the grafted Au_{0.4}Pt_{0.6}-CNT samples with Pt(0) as the core and a Au(I)/Pt($\delta+$)-thiolate complex as the shell.

F. XPS characterization of annealed ligand-free Au_{0.4}Pt_{0.6}-CNT-A

The dominant peak in the Pt 4f spectrum of the Au_{0.4}Pt_{0.6}-CNT-A (Fig. 1h) at 72.0 eV (Pt($\delta+$)) shows a negative shift of ~ 0.7 eV, relative to 72.7 eV (Pt($\delta+$)) in the Au_{0.4}Pt_{0.6}-CNT spectrum. Similarly, the dominant peak in the Au 4f spectrum of the Au_{0.4}Pt_{0.6}-CNT-A sample (Fig. 1h and Table S3) at 83.7 eV (Au(0)) shows a negative shift of ~ 0.8 eV, relative to the peak at 84.5 eV in Au_{0.4}Pt_{0.6}-CNT; the peak at 70.9 eV of the Pt 4f_{7/2} spectrum can be assigned to Pt(0) [42], suggesting an increased metallic character of the AuPt NCs on CNTs after annealing. The presence of the Pt(0) peak and the increased intensity of the Pt($\delta+$) in the alloyed vs the pure Pt sample suggests the existence of both a pure Pt phase and an AuPt alloyed phase. In combination with the other results showed later in this paper, we take this as a strong indication that the structure of the AuPt NCs is that of a Pt core surrounded by an AuPt shell. Besides, the Au_{0.4}Pt_{0.6}-CNT-A XPS shows a high content of S-O bonds, with a dominant S 2p_{3/2} peak at 167.91 eV, and a severely diminished presence of S in thiol groups (Fig. S11 and Table S2). This is a strong indication of the breakdown during annealing of the thiol groups initially attached to the AuPt NCs. A significant amount of FeS₂ and very minor AuS/PtS components are also identified in the XPS analysis, at binding energies of 161.85 eV and 165.83 eV, respectively. Low amounts of PtO and PtO₂ were observed in the ligand-free Au_{0.4}Pt_{0.6}-CNT-A sample due to surface oxidation.

G. XANES characterizations

To further confirm the oxidation state of Pt in the Au_{0.4}Pt_{0.6}-CNT-A sample, XANES spectra (Figs. 1i and S14) were also collected. The Pt L₂ and Pt L₃ edges show that the Au_{0.4}Pt_{0.6}-CNT and Au_{0.4}Pt_{0.6}-CNT-A samples display similar patterns as Pt foil, indicating that the Pt element in all the samples is mostly in metallic state, confirming Pt(0) in the core of both Au_{0.4}Pt_{0.6}-CNT and Au_{0.4}Pt_{0.6}-CNT-A, which is consistent

with the XPS results of Pt 4f spectra (Fig. 1h). For the Pt L₂ edge, the white line is significantly higher for the ligand-free AuPt (Pt)-CNT-A samples than for the Pt foil, which means there are some empty Pt d_{3/2} states close to the Fermi level, which may be the oxidized state of Pt. This is consistent with the XPS results. The (ligand-protected) AuPt-CNT shows a higher white line than (ligand-free) AuPt-CNT-A, suggesting the dominant features of AuPt-CNT are situated between those of the Pt foil (Pt(0)) and PtO₂ (Pt(IV)).

H. Effect of varying composition on the results

We explore different structures of the AuPt-CNT-A samples by varying the atomic Au/Pt ratios. The nominal compositions of pure (ligand-protected) Au, Au_{0.8}Pt_{0.2}, Au_{0.4}Pt_{0.6}, Au_{0.2}Pt_{0.8}, and pure Pt NCs as the precursors are achieved by varying the HAuCl₄ to H₂PtCl₆ ratios in the reaction mixture, respectively. TEM images of these samples are shown in Fig. 2a and Figs. S15-17. The corresponding size distribution of the discrete NCs is as shown in Fig. 2b, indicating average sizes of ~ 1.5 nm for Au, Au_{0.4}Pt_{0.6}, Au_{0.2}Pt_{0.8}, and pure Pt NCs. The size distribution of Au_{0.8}Pt_{0.2} NCs peaks at a slightly larger value, ~ 2.5 nm. The NC sizes in the (ligand-protected) Au-CNT, Au_{0.4}Pt_{0.6}-CNT, Au_{0.2}Pt_{0.8}-CNT, the Pt-CNT samples (Fig. 2a and Figs. S18-20) are similar to those before grafting. From the inductively coupled plasma (ICP) analysis (Table S6), the (ligand-free) AuPt-CNT-A films with an atomic Au fraction $x_{\text{Au}} = 1, 0.56, 0.68, 0.34, 0.143,$ and 0 correspond to the nominal compositions of Au-CNT-A, Au_{0.8}Pt_{0.2}-CNT-A, Au_{0.6}Pt_{0.4}-CNT-A, Au_{0.4}Pt_{0.6}-CNT-A, Au_{0.2}Pt_{0.8}-CNT-A and Pt-CNT-A, respectively (Fig. 2c). Recall that the nominal compositions are proportional to the relative concentration of HAuCl₄ in the reaction mixture, but this may deviate slightly from the ICP measured values. Moreover, the pure Au-CNT-A and Pt-CNT-A samples (depicted in Figs. S21-22) show similar morphology to the grafted CNT films, demonstrating that the samples retain their overall morphology after annealing.

To investigate the dependence of the electronic structure on the atomic Au/Pt ratios in the AuPt-CNT-A films, we measured their XPS spectra (Figs. S23-24). The main peak position in the Au 4f_{7/2} spectra shifted from 84.06 down to 84.04, 83.84, 83.64, and 83.48 eV as the Au/Pt ratio was reduced, which indicates the synergistic effect of Au and Pt. The Au 4f_{7/2} spectrum of the Au_{0.4}Pt_{0.6}-CNT-A film negatively shifted by about -0.42 eV compared with Au-CNT-A, whereas the Pt 4f_{7/2} spectrum of the same sample shifted positively by about $+0.24$ eV compared with Pt-CNT-A, revealing the nature of the electronic interaction between Au and Pt in Au_{0.4}Pt_{0.6}-CNT-A, with Au being a slightly more electronegative species than Pt. Additionally, by normalizing the relative sensitivity factors of the Pt 4f_{7/2} spectra, the average composition (Table S7) indicates that the proportion of Pt(0)/Pt(δ^+) increases with decreasing Au:Pt atomic ratio for the annealed samples. It is also clear that the diminishing binding energy of Pt(0) as the Au atomic ratio increases suggests that the Au/Pt atomic ratio can be used to modulate the electronic structure of the NCs.

I. Simulated-annealing molecular dynamics

We carried out a series of atomistic simulations to understand the structure and electrocatalytic activity of the NCs. The simulations are carried out with a purposely trained machine learning interatomic potential (MLP) [44] for the Au-Pt-H system. We start by generating structural models of the ligand-free AuPt NCs. According to the size-distribution estimates from experiment, the ligand-free NCs containing circa 350 metal atoms are the most representative, and so we focus on this size range. We use a high-temperature simulated-annealing procedure to survey 11 compositions with different Au fraction at 7 different annealing temperatures, and 10 structures per combination (for a total of 770 ligand-free NCs) [45, 46].

The end structures are obtained via a sequence of three steps: high-temperature annealing, quench to low temperature and optimization to the nearest local minimum of the potential energy surface. The library of structures, as well as the MLP, have been made available via Zenodo [47, 48]. With the lowest-energy ligand-free NCs per composition, we reconstruct the convex hull of stability for the AuPt system, shown in Fig. 2d. In the plot, the formation energies of the alloy NCs are computed with respect to a reference formation energy linearly interpolated from the pure Pt and Au values. The convex hull is defined by the ‘‘simplest’’ curve that contains all data points from below, going from $x = 0$ to $x = 1$. We see from the small energy differences that stable structures can be obtained for all values of Au fraction x , with a slight reduction in relative stability at $x \sim 0.2$ of up to 10 meV/atom, which is still significantly lower than the thermal kinetic energy per atom available at room temperature (~ 39 meV). We further note that this is a potential energy analysis, and that the alloys would be further stabilized by the entropic contribution if looking at the Gibbs free energy of formation instead.

At every composition we select the lowest-energy NC for further structural analysis, and to carry out the hydrogenation simulations. A very obvious structural feature of these NCs is the strong segregation of Au atoms towards the surface. Fig. 2e shows the percentage of Au atoms among the surface and subsurface atoms, determined with a stochastic probe-sphere algorithm [49]. At all compositions, a strong increase in the amount of Au atoms at the surface is observed, compared to the amount expected from the nominal NC composition. At the same time, a very strong depletion of subsurface Au atoms takes place. This means that, even for NCs as small as these, where as many as 200 atoms out of 350 are at the surface, the NCs are almost entirely covered by Au atoms at and above 60 % Au content. This confirms the core/shell structure of the AuPt NCs after annealing observed experimentally. In the NCs with low Au fraction there is a clear prediction for a Pt(core)/AuPt(shell) structure, in accordance with our experimental XPS analysis of ligand-free AuPt-CNT-A.

J. Electrocatalytic performance of AuPt-CNT-A for HER

Figs. 3a and g show the polarization curves of the samples at different Au/Pt ratios and the schematic illustration of the

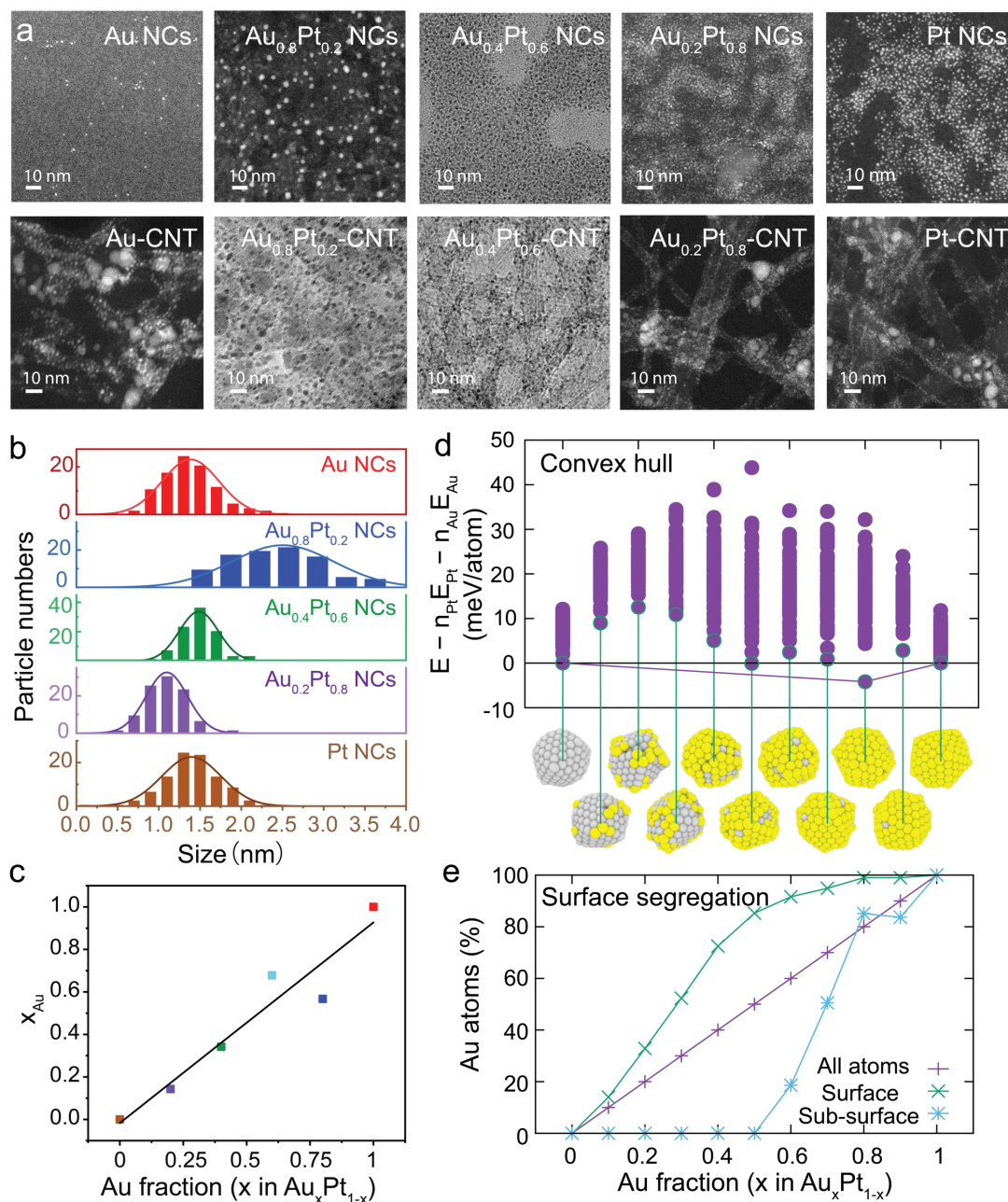


FIG. 2. a) STEM BF/DF images of AuPt NCs and AuPt-CNT with various precursor ratios in the reaction mixture. AuPt NCs show bright contrast in dark-field view. Vice versa, AuPt NCs show dark contrast in bright-field view. b) Corresponding particle-size statistics of AuPt NCs. c) Atomic Au fraction as the function of the Au-precursor (HAuCl₄) concentration present in AuPt-CNT. d) Convex-hull reconstruction of AuPt NCs with 350 atoms as a function of composition. At each composition, 70 candidate NPs are generated and the lowest in energy is chosen to draw the convex hull. These low-energy NCs are also depicted below. e) Percentage of Au surface and subsurface atoms in the low-energy NCs, as a function of composition.

electrochemical cell setup in a 0.5 M H₂SO₄ electrolyte, respectively. The pristine CNTs and sulfated CNTs are inactive for HER, indicating that the Fe catalyst plays a negligible role in HER (Fig. S28). Interestingly, the highest catalytic activity is shown by Au_{0.4}Pt_{0.6}-CNT-A, exhibiting low overpotentials of 25 and 89 mV at the cathodic current densities of 10 and

100 mA cm⁻² (Figs. 3a-b), respectively, which is comparable to, or even smaller than, those of many reported noble-metal catalysts (Fig. 3h and Table S8). It is superior to both Pt-CNT-A or Au-CNT-A, revealing the synergistic enhancement of the catalytic activity between Au and Pt in HER. Furthermore, to investigate how the catalytic activity is affected by different ra-

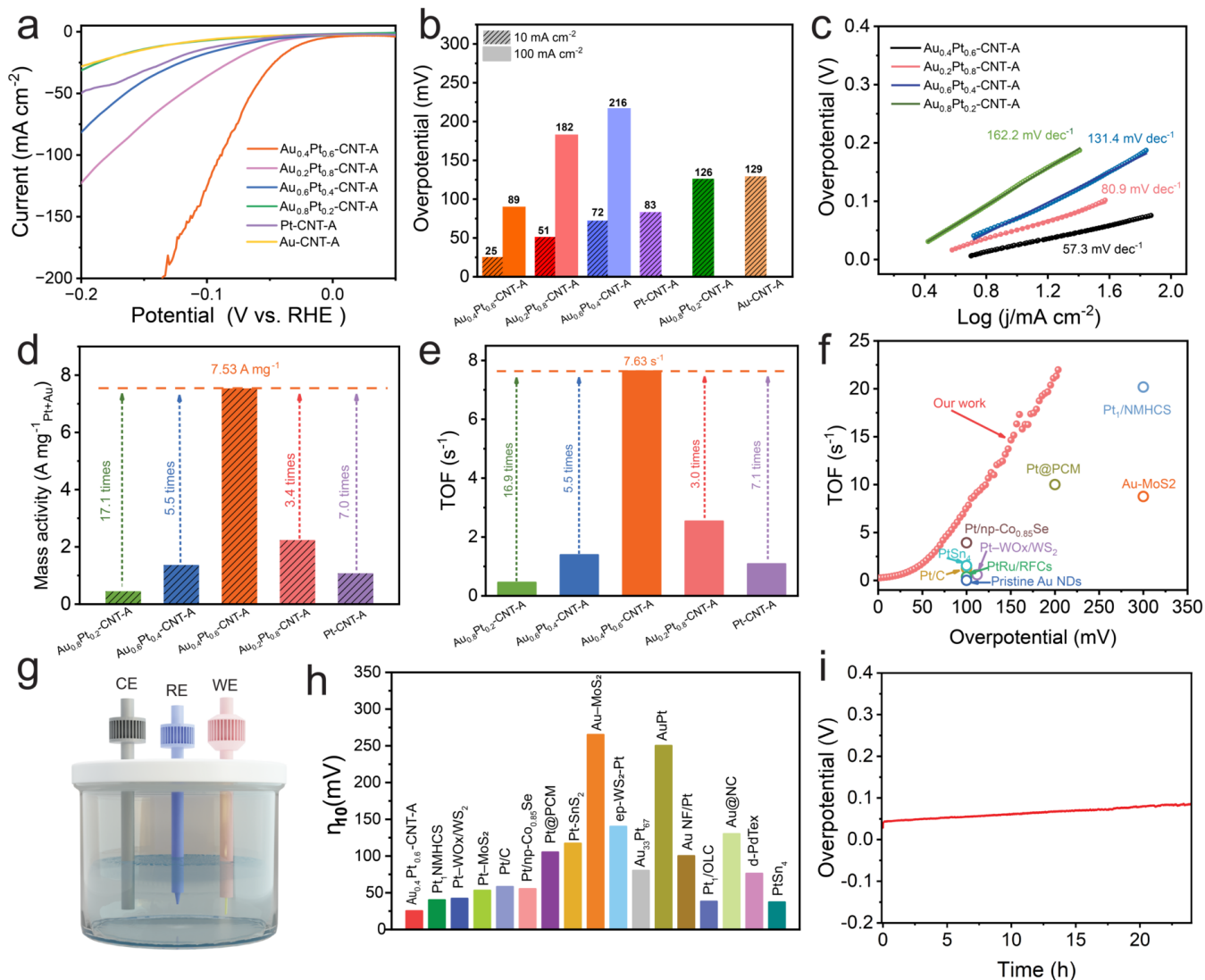


FIG. 3. a) Linear sweep voltammetry (LSV) plots of Au-CNT-A, Au_{0.8}Pt_{0.2}-CNT-A, Au_{0.6}Pt_{0.4}-CNT-A, Au_{0.4}Pt_{0.6}-CNT-A, Au_{0.2}Pt_{0.8}-CNT-A, and Pt-CNT-A. b) Overpotentials of catalysts at 10 mA cm⁻² and 100 mA cm⁻². c) Tafel plots of Au_{0.4}Pt_{0.6}-CNT-A and the control samples. d) Mass activity at the overpotential of 100 mV in comparison with those of Au_{0.8}Pt_{0.2}-CNT-A, Au_{0.6}Pt_{0.4}-CNT-A, Au_{0.2}Pt_{0.8}-CNT-A. e) The turnover frequency (TOF) at the overpotential of 100 mV of Au_{0.8}Pt_{0.2}-CNT-A, Au_{0.6}Pt_{0.4}-CNT-A, Au_{0.4}Pt_{0.6}-CNT-A, Au_{0.2}Pt_{0.8}-CNT-A, and Pt-CNT-A. f) Comparison of TOF of Au_{0.8}Pt_{0.2}-CNT-A with recent research. g) Schematic illustration of hydrogen evolution reaction. h) Comparison of the overpotential of Au_{0.8}Pt_{0.2}-CNT-A with recent research. i) Chronoamperometric measurement of Au_{0.4}Pt_{0.6}-CNT-A. All tests are performed in N₂-saturated 1.0 M H₂SO₄ solutions.

tios of Au/Pt, the polarization curves were also performed on Au_{0.8}Pt_{0.2}-CNT-A, Au_{0.6}Pt_{0.4}-CNT-A, and Au_{0.2}Pt_{0.8}-CNT-A (Fig. 3a). As shown in Fig. 3b, the overpotentials required to drive the Au_{0.8}Pt_{0.2}-CNT-A cathodic current densities of 10 and 100 mA cm⁻² are 126 and 281 mV, respectively; for Au_{0.6}Pt_{0.4}-CNT-A they are 72 and 216 mV; and for Au_{0.2}Pt_{0.8}-CNT-A they are 51 and 182 mV. Therefore, among the available samples, Au_{0.4}Pt_{0.6}-CNT-A shows the highest activity, revealing the optimal concentration of Au to enhance the HER catalytic performance. Therefore, the high intrinsic activity of Pt can be further increased by tuning the geometric and electronic structure of AuPt NCs via surface segregation of the Au atoms, which is confirmed by XPS and XANES analysis and

MD simulations (Figs. 1g-h, and Figs. 2d-e). The activity of Pt atoms towards H adsorption increases (by lowering the overpotential) when these are surrounded by Au atoms at the NC facets. A full mechanistic picture of this process is presented below through H adsorption simulations at variable chemical potential with the MLP. Fig. 3c displays the Tafel plots (log j vs η) of the HER and shows that Au_{0.4}Pt_{0.6}-CNT-A exhibited a small corresponding Tafel slope of 57.3 mV dec⁻¹, suggesting that the HER on this catalyst is also dominated by the Tafel mechanism (H_{ads} + H_{ads} → H₂ ↑). In contrast, the Au_{0.8}Pt_{0.2}-CNT-A, Au_{0.6}Pt_{0.4}-CNT-A, and Au_{0.2}Pt_{0.8}-CNT-A samples have Tafel slopes of 162.2, 131.4, and 80.7 mV dec⁻¹, respectively. This confirms that Au_{0.4}Pt_{0.6}-CNT-A has a much

faster HER kinetics than NC with other Au/Pt ratios. The Tafel slopes of the CNTs (figure S28) are $143.2 \text{ mV dec}^{-1}$, indicating the slow kinetics of CNT for HER without nanoclusters. The electrochemical impedance spectroscopy (EIS) analysis further demonstrates the enhanced HER kinetics in the 0.5 M H_2SO_4 electrolyte (Figs. S25-26). The charge transfer resistance (R_{ct}) is listed in Table S9. $\text{Au}_{0.4}\text{Pt}_{0.6}$ -CNT-A shows a much lower R_{ct} (0.25Ω) than those of $\text{Au}_{0.2}\text{Pt}_{0.8}$ -CNT-A ($R_{\text{ct}} = 0.5\Omega$), Pt-CNT-A (1.14Ω), and Au-CNT-A (3.25Ω), indicating that $\text{Au}_{0.4}\text{Pt}_{0.6}$ -CNT-A has an improved electron transport kinetics compared to Pt-CNT-A and Au-CNT-A. The enhanced catalytic activity can be attributed to the modified electronic structure of the Pt surface sites on $\text{Au}_{0.4}\text{Pt}_{0.6}$ NCs and their increased ability to bind hydrogen, as will be explained in detail below in the context of our atomistic simulations.

The ECSAs of the $\text{Au}_{0.4}\text{Pt}_{0.6}$ -CNT-A and referenced samples are shown in Fig. S27. The corresponding electric double-layer capacitance (C_{dl}) value of $\text{Au}_{0.4}\text{Pt}_{0.6}$ -CNT-A is close to that of other samples, indicating the catalysts have similar number of active sites. Besides, as shown in Fig. 3d, $\text{Au}_{0.4}\text{Pt}_{0.6}$ -CNT-A has a high mass activity [6] of 7.53 A mg^{-1} at $\eta = 100 \text{ mV}$, which is 3.4, 5.5, 7, and 17.1 times that of the $\text{Au}_{0.2}\text{Pt}_{0.8}$ -CNT-A, $\text{Au}_{0.6}\text{Pt}_{0.4}$ -CNT-A, Pt-CNT-A, and $\text{Au}_{0.8}\text{Pt}_{0.2}$ -CNT-A samples, respectively, indicating an intrinsic HER activity of $\text{Au}_{0.4}\text{Pt}_{0.6}$ -CNT-A higher than that of AuPt-CNT-A with other Au/Pt ratios.

As shown in Fig. 3e, the turnover frequency (TOF) of the $\text{Au}_{0.4}\text{Pt}_{0.6}$ -CNT-A sample at $\eta = 100 \text{ mV}$ is 7.63 s^{-1} , which outperforms the other bimetallic samples with different Au/Pt ratios studied here as well as the majority of reported Au- and Pt-based catalysts from the literature (Fig. 3f and Table S10), further indicating that the Au atoms could work as an enhancer for the intrinsic activity of Pt in $\text{Au}_{0.4}\text{Pt}_{0.6}$ -CNT-A by modulate the electronic structure of the ligand-free NCs on CNT.

It should be noted that, prior to annealing, the $\text{Au}_{0.4}\text{Pt}_{0.6}$ -CNT sample (Fig. S28) performed far worse than the ligand-free $\text{Au}_{0.4}\text{Pt}_{0.6}$ -CNT-A sample did. A significantly enhanced catalytic activity can be observed after annealing, demonstrating that the ligand-removal process plays a crucial role in HER enhancement. At the same time, the grafted (ligand-protected) $\text{Au}_{0.4}\text{Pt}_{0.6}$ -CNT shows a higher R_{ct} than annealed ligand-free $\text{Au}_{0.4}\text{Pt}_{0.6}$ -CNT-A, and also shows low ECSAs, suggesting the annealing process can remove the catalytically inert organic groups on the NC surface, whilst optimizing the NC bimetallic structure. For comparison, as shown in Fig. S29, the annealed $\text{Au}_{0.4}\text{Pt}_{0.6}$ NCs without the support of CNT agglomerated. This suggests the CNT film promotes the uniform distribution of $\text{Au}_{0.4}\text{Pt}_{0.6}$ NCs and prevents agglomeration, thus maximizing the exposure of active sites. Besides, as shown in Fig. S30, the polarization curves of pure ligand-protected $\text{Au}_{0.4}\text{Pt}_{0.6}$ NCs prior to grafting on the CNTs and annealing show a high overpotential and low mass activity (0.0376 A mg^{-1}), which indicates a low HER activity of the ligand-protected $\text{Au}_{0.4}\text{Pt}_{0.6}$ NCs.

The durability of the $\text{Au}_{0.4}\text{Pt}_{0.6}$ -CNT-A sample is examined by a chronoamperometric measurement (Fig. 3i) at 10 mA cm^{-2} over 24 h without significant variation in over-

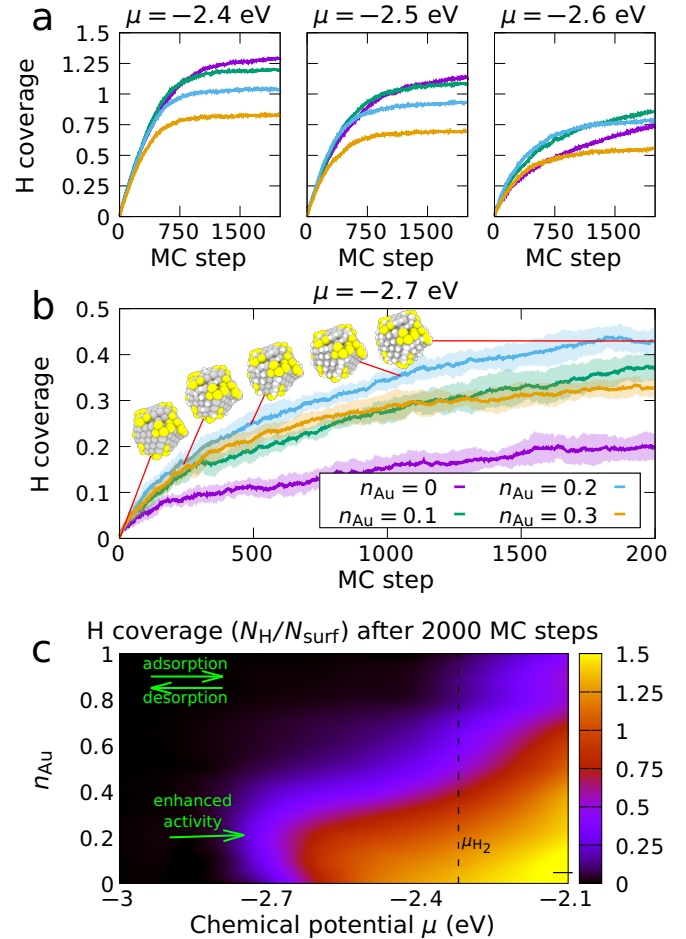
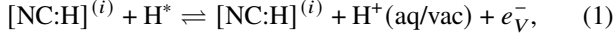


FIG. 4. a) Example MCMC runs (each an average over 10 individual MCMC trajectories) for 0, 10, 20 and 30 % Au content (legend in b). b) Detailed MCMC run at $\mu = -2.7 \text{ eV}$, where the shaded areas indicate the statistical error (standard deviation) from averaging over the 10 individual trajectories per composition. The inset NC snapshots show the location of the adsorbed hydrogens at different stages for a particular trajectory at 20 % Au content. c) Coverage after 2000 MCMC steps as a function of composition and chemical potential. Adsorption is favored as one increases the chemical potential and desorption is favored in the opposite direction. The chemical potential of H_2 (half of the cohesive energy of the H_2 molecule) is indicated with a vertical line. The region of increased activity at around 20 % Au content is also indicated. All panels use the ratio of adsorbed hydrogens N_{H} to surface metal atoms N_{surf} as the definition of coverage.

potential, suggesting the $\text{Au}_{0.4}\text{Pt}_{0.6}$ -CNT-A film electrode is stable for HER catalysis in acid solution during a long-term durability test. The Au 4f and Pt 4f XPS spectra were also measured for this sample post chronoamperometric measurement, showing slightly oxidized Pt on the surface of the $\text{Au}_{0.4}\text{Pt}_{0.6}$ -CNT-A film (Fig. S31).

K. Atomistic hydrogenation simulations

To elucidate the hydrogen adsorption mechanism in the ligand-free bimetallic AuPt NCs and its relation to the enhanced HER activity observed experimentally, we carry out heuristic Markov-chain Monte Carlo (MCMC) simulations. In brief, we allow the addition and removal of adsorbed hydrogen atoms until the following equilibrium is reached, for a given potential V :



that is, at step i (after sufficiently many steps), the (free) energy difference between hydrogen adsorption and desorption is zero. For hydrogen desorption, the free energy of the proton μ_{H^+} is given by a chemical reservoir (in aqueous or vacuous environment) and the free energy of the electron $-eV$ is given by the electrochemical potential V . Within our methodological framework, this is the same as defining an effective chemical potential for the neutral hydrogen species given by $\mu_{\text{H}} = \mu_{\text{H}^+} - eV$. Since μ_{H^+} is fixed, we can mimic the effect of tuning V during the experiment by tuning μ_{H} in the simulation. More details about these simulations are given in the Supplemental Information. Examples of MCMC trajectories for some of the most interesting cases are given in the top and middle panels of Fig. 4. Fig. 4b also provides error estimates based on the statistics of 10 independent runs per composition and chemical potential. At high chemical potential (low electrode potential) the activity towards hydrogen adsorption goes down as the Au fraction increases, as expected. However, as the chemical potential is decreased, one can see an enhancement of the hydrogenation activity at $x \sim 0.2$. Fig. 4b shows a few snapshots along one of the trajectories at $\mu = -2.7$ eV and $x = 0.2$, where it is clear that H preferentially adsorbs on or between Pt atoms, including a visible (111)-like facet where the hydrogens adopt the familiar on-top configuration. Remarkably, the presence of nearby Au atoms works as an enhancer for the reactivity on the Pt atoms, and indeed H adsorption is more favorable on the ligand-free bimetallic $\text{Au}_x\text{Pt}_{1-x}$ NCs with $x \sim 0.2$ than on the pure ligand-free metallic Pt NCs at low chemical potential, or high electrode potential, in excellent qualitative agreement with the trends observed in experiment, although the nominal composition of the optimum in experiment is higher than in the simulation results. Fig. 4c provides a more general view of the effect described here.

More insight into the mechanistic understanding of this enhancement can be obtained by looking back at Fig. 2d. We see that the relative cohesive energy per atom is lowest in the ligand-free bimetallic AuPt with a low content of Au. Therefore, within this range of compositions the ligand-free metallic NCs is more susceptible to lower its cohesive energy via creation of bonds with adsorbed hydrogen. Thus, the Au-mediated enhancement of the Pt reactivity towards hydrogen adsorption at high electrode potentials is achieved by creating a slightly less stable NC surface. However, this process only works at low Au content because a significant number of Pt surface atoms still need to be available on the surface, given the inability of Au to efficiently bind hydrogen at high electrode potentials.

IV. CONCLUSION

In summary, we synthesized a series of high-dispersion and ligand-free AuPt bimetallic nanoclusters-CNT-A complex by grafting nanoclusters on CNT film and subsequently annealing. We created ligand-free nanoclusters with a unique core (Pt)-shell (AuPt) structure. Pt atom exposure on the outer surface enhances the electrocatalytic activity for hydrogen evolution reaction (HER) in aqueous media via a synergistic effect between Pt and Au atoms. As revealed by molecular dynamics simulations, the core (Pt)-shell (AuPt) structure of the annealed AuPt NCs at a low Au fraction is achieved through an almost complete Au surface segregation. At low-enough Au fraction, a sufficient number of catalytically active Pt sites remain exposed on the surface. The ligand-free $\text{Au}_{0.4}\text{Pt}_{0.6}$ nanoclusters-CNT-A complex shows the highest HER activity among all nanoclusters, with an overpotential of 27 mV at 10 mA cm^{-2} , a high mass activity of 7.49 A mg^{-1} at $\eta = 100$ mV, and a high TOF of 7.63 s^{-1} , outperforming the majority of reported Pt-based catalysts. Markov-chain Monte Carlo simulations with a custom-made machine-learning potential indicate that the Au atoms work as an enhancer for the reactivity on Pt atoms, where H adsorption is more favorable on AuPt at a low Au fraction than on pure Pt. The enhanced HER activity together with the stability obtained by grafting on the CNT support show great promise for efficient production of hydrogen. Furthermore, the elucidation of the atomistic mechanism leading to this anomalous enhancement provides insight into useful design principles to increase the catalytic activity of Pt-based nanomaterials with HER-inactive atoms at the atomic level [50], with potential extensions to other materials.

SUPPORTING INFORMATION

The supporting information contains details of both the experimental characterization and the atomistic simulations.

ACKNOWLEDGMENTS

We acknowledge funding from the Research Council of Finland (B. P.: no. 321443 and 352671; O. I.: Center of Excellence Program in Life-inspired Hybrid Materials, LIBER, no. 346108; Z.-P. L: no. 330214), China Scholarship Council (J. Kang: no. 202008440308, J.S.: no. 202008440311, Z.X: no. 202008440534). We also thank Ville Liljeström for conducting the WAXS/SAXS measurements. Use of facilities and technical support were provided by the Aalto University OtaNano-Nanomicroscopy Center, Bioeconomy Infrastructure, and Raw Materials Research Infrastructures. J. Kloppeburg and M. A. C. acknowledge financial support from the Research Council of Finland under grants nos. 329483, 330488 and 347252, as well as computational resources from CSC (the Finnish IT Center for Science) and Aalto University's Science-IT Project. We thank Shun Yu for assisting with the beam time proposal. We acknowledge the MAX IV

Laboratory for time in the BALDER beamline under Proposal 20220785. We thank Konstantin Klementiev for the XANES measurement and valuable discussions.

REFERENCES

- [1] Z. W. Seh, J. Kibsgaard, C. F. Dickens, I. Chorkendorff, J. K. Nørskov, and T. F. Jaramillo, "Combining theory and experiment in electrocatalysis: Insights into materials design," *Science* **355**, eaad4998 (2017).
- [2] M. P. Browne, Z. Sofer, and M. Pumera, "Layered and two dimensional metal oxides for electrochemical energy conversion," *Energy Environ. Sci.* **12**, 41 (2019).
- [3] C. Hu, L. Zhang, and J. Gong, "Recent progress made in the mechanism comprehension and design of electrocatalysts for alkaline water splitting," *Energy Environ. Sci.* **12**, 2620 (2019).
- [4] L. Li, P. Wang, Q. Shao, and X. Huang, "Recent progress in advanced electrocatalyst design for acidic oxygen evolution reaction," *Adv. Mater.* **33**, 2004243 (2021).
- [5] L. Han, S. Dong, and E. Wang, "Transition-metal (Co, Ni, and Fe)-based electrocatalysts for the water oxidation reaction," *Adv. Mater.* **28**, 9266 (2016).
- [6] C. Zhu, Q. Shi, S. Feng, D. Du, and Y. Lin, "Single-atom catalysts for electrochemical water splitting," *ACS Energy Lett.* **3**, 1713 (2018).
- [7] B. Zhang, X. Zheng, O. Voznyy, R. Comin, M. Bajdich, M. García-Melchor, L. Han, J. Xu, M. Liu, F. P. Zheng, L. García de Arquer, C. T. Dinh, F. Fan, M. Yuan, E. Yassitepe, N. Chen, T. Regier, P. Liu, Y. Li, P. De Luna, A. Janmohamed, H. L. Xin, H. Yang, A. Vojvodic, and E. H. Sargent, "Homogeneously dispersed multimetal oxygen-evolving catalysts," *Science* **352**, 333 (2016).
- [8] X. Zou and Y. Zhang, "Noble metal-free hydrogen evolution catalysts for water splitting," *Chem. Soc. Rev.* **44**, 5148 (2015).
- [9] K. Jiang, B. Liu, M. Luo, S. Ning, M. Peng, Y. Zhao, Y.-R. Lu, T.-S. Chan, F. M. F. de Groot, and Y. Tan, "Single platinum atoms embedded in nanoporous cobalt selenide as electrocatalyst for accelerating hydrogen evolution reaction," *Nature Commun.* **10**, 1743 (2019).
- [10] H. Zhang, P. An, W. Zhou, B. Y. Guan, P. Zhang, J. Dong, and X. W. Lou, "Dynamic traction of lattice-confined platinum atoms into mesoporous carbon matrix for hydrogen evolution reaction," *Sci. Adv.* **4**, eaao6657 (2018).
- [11] S. Sanati, A. Morsali, and H. García, "First-row transition metal-based materials derived from bimetallic metal-organic frameworks as highly efficient electrocatalysts for electrochemical water splitting," *Energy Environ. Sci.* **15**, 3119 (2022).
- [12] R. Jin, "Atomically precise metal nanoclusters: stable sizes and optical properties," *Nanoscale* **7**, 1549 (2015).
- [13] Y. Chen, C. Zeng, D. R. Kauffman, and R. Jin, "Tuning the magic size of atomically precise gold nanoclusters via isomeric methylbenzenethiols," *Nano Lett.* **15**, 3603 (2015).
- [14] C. Zeng, Y. Chen, A. Das, and R. Jin, "Transformation chemistry of gold nanoclusters: from one stable size to another," *J. Phys. Chem. Lett.* **6**, 2976 (2015).
- [15] K. D. Gilroy, A. Ruditskiy, H.-C. Peng, D. Qin, and Y. Xia, "Bimetallic nanocrystals: syntheses, properties, and applications," *Chem. Rev.* **116**, 10414 (2016).
- [16] Y.-J. Wang, N. Zhao, B. Fang, H. Li, X. T. Bi, and H. Wang, "Carbon-supported pt-based alloy electrocatalysts for the oxygen reduction reaction in polymer electrolyte membrane fuel cells: particle size, shape, and composition manipulation and their impact to activity," *Chem. Rev.* **115**, 3433 (2015).
- [17] M. Sankar, N. Dimitratos, P. J. Miedzziak, P. P. Wells, C. J. Kiely, and G. J. Hutchings, "Designing bimetallic catalysts for a green and sustainable future," *Chem. Soc. Rev.* **41**, 8099 (2012).
- [18] Y. Xia, Y. Xiong, B. Lim, and S. E. Skrabalak, "Shape-controlled synthesis of metal nanocrystals: simple chemistry meets complex physics?" *Angew. Chem. Int. Ed.* **48**, 60 (2009).
- [19] J. F. Li, Y. F. Huang, Y. Ding, Z. L. Yang, S. B. Li, X. S. Zhou, F. R. Fan, W. Zhang, Z. Y. Zhou, D. Y. Wu, B. Ren, Z. L. Wang, and Z. Q. Tian, "Shell-isolated nanoparticle-enhanced Raman spectroscopy," *Nature* **464**, 392 (2010).
- [20] K. Zhou and Y. Li, "Catalysis based on nanocrystals with well-defined facets," *Angew. Chem. Int. Ed.* **51**, 602 (2012).
- [21] Y. Yao, Z. Huang, P. Xie, S. D. Lacey, R. J. Jacob, H. Xie, F. Chen, A. Nie, T. Pu, M. Rehwoldt, D. Yu, M. R. Zachariah, C. Wang, R. Shahbazian-Yassar, J. Li, and L. Hu, "Carbothermal shock synthesis of high-entropy-alloy nanoparticles," *Science* **359**, 1489 (2018).
- [22] T. Chen and V. O. Rodionov, "Controllable catalysis with nanoparticles: bimetallic alloy systems and surface adsorbates," *ACS Catal.* **6**, 4025 (2016).
- [23] L. Xu, H.-W. Liang, Y. Yang, and S.-H. Yu, "Stability and reactivity: positive and negative aspects for nanoparticle processing," *Chem. Rev.* **118**, 3209 (2018).
- [24] F. Wang, K. Kusada, D. Wu, T. Yamamoto, T. Toriyama, S. Matsumura, Y. Nanba, M. Koyama, and H. Kitagawa, "Solid-solution alloy nanoparticles of the immiscible iridium-copper system with a wide composition range for enhanced electrocatalytic applications," *Angew. Chem. Int. Ed.* **57**, 4505 (2018).
- [25] H. Qian, D.-E. Jiang, G. Li, C. Gayathri, A. Das, R. R. Gil, and R. Jin, "Monoplatinum doping of gold nanoclusters and catalytic application," *J. Am. Chem. Soc.* **134**, 16159 (2012).
- [26] S. Xie, H. Tsunoyama, W. Kurashige, Y. Negishi, and T. Tsukuda, "Enhancement in aerobic alcohol oxidation catalysis of Au₂₅ clusters by single Pd atom doping," *ACS Catal.* **2**, 1519 (2012).
- [27] C. A. Fields-Zinna, M. C. Crowe, A. Dass, J. E. F. Weaver, and R. W. Murray, "Mass spectrometry of small bimetal monolayer-protected clusters," *Langmuir* **25**, 7704 (2009).
- [28] B. Liu, H. Yao, W. Song, L. Jin, I. M. Mosa, J. F. Rusling, S. L. Suib, and J. He, "Ligand-free noble metal nanocluster catalysts on carbon supports via "soft" nitriding," *J. Am. Chem. Soc.* **138**, 4718 (2016).
- [29] Y. Shao, G. Yin, Y. Gao, and P. Shi, "Durability study of Pt/C and Pt/CNTs catalysts under simulated PEM fuel cell conditions," *J. Electrochem. Soc.* **153**, A1093 (2006).
- [30] K. Liu, W. Wang, Z. Xu, X. Bai, E. Wang, Y. Yao, J. Zhang, and Z. Liu, "Chirality-dependent transport properties of double-walled nanotubes measured in situ on their field-effect transistors," *J. Am. Chem. Soc.* **131**, 62 (2009).
- [31] A. B. A. A. Nassr, I. Sinev, M.-M. Pohl, W. Grunert, and M. Bron, "Rapid microwave-assisted polyol reduction for the preparation of highly active PtNi/CNT electrocatalysts for methanol oxidation," *ACS Catal.* **4**, 2449 (2014).
- [32] Z. Luo, X. Yuan, Y. Yu, Q. Zhang, D. T. Leong, J. Y. Lee, and J. Xie, "From aggregation-induced emission of Au(I)-thiolate complexes to ultrabright Au(0)@Au(I)-thiolate core-shell nanoclusters," *J. Am. Chem. Soc.* **134**, 16662 (2012).
- [33] Y. Shi and B. Zhang, "Recent advances in transition metal phosphide nanomaterials: synthesis and applications in hydrogen evolution reaction," *Chem. Soc. Rev.* **45**, 1529 (2016).
- [34] G. D. Park and Y. C. Kang, "Multiroom-structured multicomponent metal selenide-graphitic carbon-carbon nanotube hybrid

- microspheres as efficient anode materials for sodium-ion batteries,” *Nanoscale* **10**, 8125 (2018).
- [35] P. Edalati, A. Mohammadi, M. Ketabchi, and K. Edalati, “Microstructure and microhardness of dual-phase high-entropy alloy by high-pressure torsion: Twins and stacking faults in FCC and dislocations in BCC,” *J. Alloys Compd.* **894**, 162413 (2022).
- [36] H. Huang, Y. Chang, J. Jia, M. Jia, and Z. Wen, “Understand the Fe₃C nanocrystalline grown on rGO and its performance for oxygen reduction reaction,” *Int. J. Hydrog. Energy* **45**, 28764 (2020).
- [37] J. Xu, T. Zhao, Z. Liang, and L. Zhu, “Facile preparation of AuPt alloy nanoparticles from organometallic complex precursor,” *Chem. Mater.* **20**, 1688 (2008).
- [38] J.-J. Feng, L.-X. Chen, X. Ma, J. Yuan, J.-R. Chen, A.-J. Wang, and Q.-Q. Xu, “Bimetallic AuPt alloy nanodendrites/reduced graphene oxide: One-pot ionic liquid-assisted synthesis and excellent electrocatalysis towards hydrogen evolution and methanol oxidation reactions,” *Int. J. Hydrog. Energy* **42**, 1120 (2017).
- [39] P. Zhang and T. K. Sham, “X-ray studies of the structure and electronic behavior of alkanethiolate-capped gold nanoparticles: the interplay of size and surface effects,” *Phys. Rev. Lett.* **90**, 245502 (2003).
- [40] X. Duan, X. Tian, J. Ke, Y. Yin, J. Zheng, J. Chen, Z. Cao, Z. Xie, and Y. Yuan, “Size controllable redispersion of sintered Au nanoparticles by using iodohydrocarbon and its implications,” *Chem. Sci.* **7**, 3181 (2016).
- [41] C. Dablemont, P. Lang, C. Mangeney, J.-Y. Piquemal, V. Petkov, F. Herbst, and G. Viau, “FTIR and XPS study of Pt nanoparticle functionalization and interaction with alumina,” *Langmuir* **24**, 5832 (2008).
- [42] T. Imaoka, Y. Akanuma, N. Haruta, S. Tsuchiya, K. Ishihara, T. Okayasu, W.-J. Chun, M. Takahashi, and K. Yamamoto, “Platinum clusters with precise numbers of atoms for preparative-scale catalysis,” *Nature Commun.s* **8**, 688 (2017).
- [43] S. L. Christensen, M. A. MacDonald, A. Chatt, P. Zhang, H. Qian, and R. Jin, “Dopant location, local structure, and electronic properties of Au₂₄Pt(SR)₁₈ nanoclusters,” *J. Phys. Chem. C* **116**, 26932 (2012).
- [44] V. L. Deringer, M. A. Caro, and G. Csányi, “Machine learning interatomic potentials as emerging tools for materials science,” *Adv. Mater.* **31**, 1902765 (2019).
- [45] J. Kloppenburg, L. B. Pártay, H. Jónsson, and M. A. Caro, “A general-purpose machine learning pt interatomic potential for an accurate description of bulk, surfaces, and nanoparticles,” *J. Chem. Phys.* **158**, 134704 (2023).
- [46] R. Jana and M. A. Caro, “Searching for iron nanoparticles with a general-purpose Gaussian approximation potential,” *Phys. Rev. B* **107**, 245421 (2023).
- [47] J. Kloppenburg and M. A. Caro, “GAP interatomic potential for PtAu:H nanoparticle simulation,” Zenodo (2024), DOI:10.5281/zenodo.11184038.
- [48] J. Kloppenburg and M. A. Caro, “Structural database of small PtAu and hydrogenated PtAu nanoparticles,” Zenodo (2024), DOI:10.5281/zenodo.11185692.
- [49] R. Ibragimova and M. A. Caro, “ase_tools: Fast Fortran libraries to be used in combination with ASE,” https://github.com/mcaroba/ase_tools (accessed January 27, 2023).
- [50] Y.-R. Zheng, P. Wu, M.-R. Gao, X.-L. Zhang, F.-Y. Gao, H.-X. Ju, R. Wu, Q. Gao, R. You, W.-X. Huang, S.-J. Liu, S.-W. Hu, J. Zhu, Z. Li, and Yu S.-H., “Doping-induced structural phase transition in cobalt diselenide enables enhanced hydrogen evolution catalysis,” *Nature Commun.* **9**, 2533 (2018).